---

**Article:**
Shandell, Mia Ann orcid.org/0000-0002-7864-758X, Quejada, Jose R., Yazawa, Masayuki et al. (2 more authors) (2019) Detection of Nav1.5 conformational change in mammalian cells using the non-canonical amino acid ANAP. Biophysical Journal. ISSN 0006-3495

https://doi.org/10.1016/j.bpj.2019.08.028

---

# Detection of $Na_v1.5$ conformational change in mammalian cells using the non-canonical amino acid ANAP

Mia A. Shandell[1†*], Jose R. Quejada[1,2], Masayuki Yazawa[1,2], Virginia W. Cornish[1,3*], Robert S. Kass[1*]

**Running Title:** Imaging $Na_v1.5$ conformational change

**Affiliations:**

1. Department of Pharmacology, College of Physicians and Surgeons, Columbia University, New York, NY, USA.
2. Department of Rehabilitation and Regenerative Medicine, Columbia Stem Cell Initiative, Columbia University, New York, NY, USA.
3. Department of Chemistry, Columbia University, New York, NY, USA.

†Current address: York Biomedical Research Institute, Hull-York Medical School, University of York, York, UK

*Corresponding authors: Mia A. Shandell, mia.shandell@york.ac.uk, Robert S. Kass, rsk20@cumc.columbia.edu, Virginia W. Cornish, vc114@columbia.edu

**Keywords**

voltage-gated sodium channels, non-canonical amino acids, ANAP

**Abstract**

$Na_v1.5$ inactivation is necessary for healthy conduction of the cardiac action potential. Genetic mutations of $Na_v1.5$ perturb inactivation and cause potentially fatal arrhythmias associated with long QT syndrome type 3. The exact structural dynamics of the

inactivation complex is unknown. To sense inactivation gate conformational change in live mammalian cells, we incorporated the solvatochromic fluorescent non-canonical amino acid ANAP into single sites in the $Na_v1.5$ inactivation gate. ANAP was incorporated in full-length and C-terminally truncated $Na_v1.5$ channels using mammalian cell synthetase-tRNA technology. ANAP-incorporated channels were expressed in mammalian cells and they exhibited pathophysiological function. A spectral imaging potassium-depolarization assay was designed to detect ANAP emission shifts associated with $Na_v1.5$ conformational change. Site-specific intracellular ANAP incorporation affords live-cell imaging and detection of $Na_v1.5$ inactivation gate conformational change in mammalian cells.

**Statement of significance**

We incorporated a fluorescent non-canonical amino acid ANAP into multiple sites within the inactivation gate of human cardiac voltage-gated sodium channels ($Na_v1.5$). We developed a fluorescence based spectral method to monitor $Na_v1.5$ conformational change in intact mammalian cells. This work compliments the near-atomic level structural detail resolved in recent cryo-EM structures of full-length eukaryotic voltage-gated sodium channels and sets the foundation for measurement of voltage-gated sodium channel structural dynamics in mammalian cells.

**Introduction**

Genetic mutation in the voltage-gated sodium channel (VGSC) $Na_v1.5$ can lead to multiple cardiac arrhythmia disorders including Brugada Syndrome and long QT syndrome type 3 (LQT3), that can both lead to sudden cardiac death. $Na_v1.5$ is a 260 kDa transmembrane ion channel with four semi-homologous domains, each containing

six transmembrane segments (1) (Figure 1a, right). The ~50 amino acid linker between domains III and IV (III-IV linker) is known as the inactivation gate. VGSC fast inactivation is thought to occur by a hinged-lid mechanism requiring the presence of a conserved hydrophobic motif, typically IFM, in the III-IV linker (1). This hydrophobic motif may stabilize a channel conformation in which the III-IV linker occludes the intracellular mouth of the pore and halts ion conduction (1–5). The IFM motif assumes a stable fast inactivated state by docking onto the underside of the pore via hydrophobic interactions, mainly with sites on the DIII:S4-S5 linker, DIV:S4-S5 linker, and DIV:S6 (5–13). The C-terminus (CT) is also important for regulating channel availability and inactivation kinetics, demonstrated by functional characterization of LQT3-associated mutations in the CT and ion channel chimera experiments (14–19). Furthermore, the inactivated state is stabilized by an interaction between the III-IV linker and CT, forming an inactivation complex, and this requires the presence of the C-terminal part of helix 6 in the CT structured region (8, 20–23).

Structures of truncated regions of eukaryotic VGSCs, such as the III-IV linker, in complex with accessory proteins have been reported; however, their functional significance is unknown (24, 25). In particular, the eukaryotic III-IV linker bound to calcium/Calmodulin (CaM) has been crystallized (24). Also, the crystal structure of the eukaryotic $Na_v1.5$ CT domain in complex with fibroblast growth factor homologous factor (FHF) and apo-CaM has been resolved (25). Considered together, these results raise questions of how the III-IV linker, CT, calcium, and CaM may interact in the inactivation complex of full-length eukaryotic channels. One limitation to the studies

supporting the significance of a direct III-IV linker CT interaction is the measurement of interactions between purified III-IV linker and CT peptides, not in full-length channels.

A number of cryo-EM structures of full-length eukaryotic VGSCs have been published to date: insect $Na_vPaS$ (26), electric eel $Na_v1.4$ (27), human $Na_v1.7$ (28), human $Na_v1.2$ (29), and hybrid $Na_vPaS$/human $Na_v1.7$ (30). Interactions between voltage sensor domain IV (VSDIV) and the CT were visualized in the full-length hybrid channel (insect $Na_vPaS$+VSDIV from human $Na_v1.7$) bound to α-scorpion toxin, suggesting a possible resting state for the fast-inactivation complex (30). One limitation of structural techniques is that there is no membrane potential in a protein crystal. Therefore, it is difficult to assign the resolved structure to voltage-dependent functional ion channel states. Fluorescence imaging in mammalian cells can be a useful complement to cryo-EM studies for connecting structure with function of the $Na_v1.5$ inactivation complex. Currently, specific fluorescent labeling of the short intracellular inactivation gate with minimal perturbation in full-length channels is a technical hurdle that must be overcome.

Options for labeling short intracellular protein linkers are limited. Fluorescent proteins are quite large and cysteine labeling is non-specific. Non-canonical amino acids (ncAAs) offer an alternative method for incorporating fluorophores at single sites in proteins by amber suppression. Amber suppression in mammalian cells requires expression of an orthogonal aminoacyl tRNA-synthetase tRNA (aaRS-tRNA) pair specific for the ncAA along with the protein of interest containing an amber stop codon at the desired incorporation site (31). ANAP (3-((6-acetylnaphthalen-2-yl)amino)-2-aminopropanoic acid) is one of a number of solvatochromic fluorescent ncAAs whose

spectrum red-shifts in increasingly polar environments (32–34) (Figure 1a, left). The ANAP aaRS-tRNA pair was evolved in *S. cerevisiae* from the *E. coli* leucyl aaRS-tRNA pair (32). Since the first demonstration of ANAP incorporation into model proteins in *S. cerevisiae* and mammalian cells, there have been a number of examples using ANAP environmental sensitivity to study ion channels in *X. laevis* oocytes and mammalian cells (35–44).

In recent years, ANAP incorporation has been used increasingly for studying protein dynamics in live cells. In 2013, Kalstrup and Blunck demonstrated voltage-clamp fluorometry (VCF) of ANAP-incorporated Shaker potassium channels in *X. laevis* oocytes and have published video protocols for reproducing ANAP VCF experiments (35, 45). ANAP spectral shifts were used to monitor protein misfolding of luciferase in *S. cerevisiae* (46). In *X. laevis* oocytes, ANAP has been incorporated into glycine receptors, CNGA1 channels, voltage-sensing phosphatases, KCNH channels, and ASIC channels (36–41). ANAP incorporated in CNGA1 and KCNH channels was used to measure intracellular interactions by transition metal FRET (tmFRET) (36). However, there is a need for characterization of ion channel structural dynamics in the mammalian cell context. A few studies have answered to that need. Zagotta *et al.* demonstrated tmFRET between ANAP incorporated in TRPV1 channels and the plasma membrane of unroofed mammalian cells (42). In CHO cells, ANAP was incorporated into hASIC1a and increasing concentrations of the channel toxin mambalgin-1 were detected spectrally by a red-shift in ANAP fluorescence (43). ANAP was demonstrated as a FRET donor to EGFP in a FP-reporter fusion protein expressed in mammalian cells

(47). Recently, Puljung *et al.* interrogated activation of ATP-sensitive $K^+$ channels in unroofed HEK293T cells via FRET between ANAP and fluorescent nucleotides (44).

We hypothesized that ANAP can be incorporated into the $Na_v1.5$ inactivation gate using mammalian cell synthetase-tRNA technology. Once incorporated, ANAP would act as a fluorescent reporter of human $Na_v1.5$ conformational change. An ANAP spectral assay was developed to address whether ANAP responds to (1) the local environment of the inactivation gate when incorporated at different sites (Figure 1b) (2) the absence of the distal CT (Figure 1b) and (3) conformational rearrangement elicited by a potassium ($K^+$)-depolarization (Figure 1c).

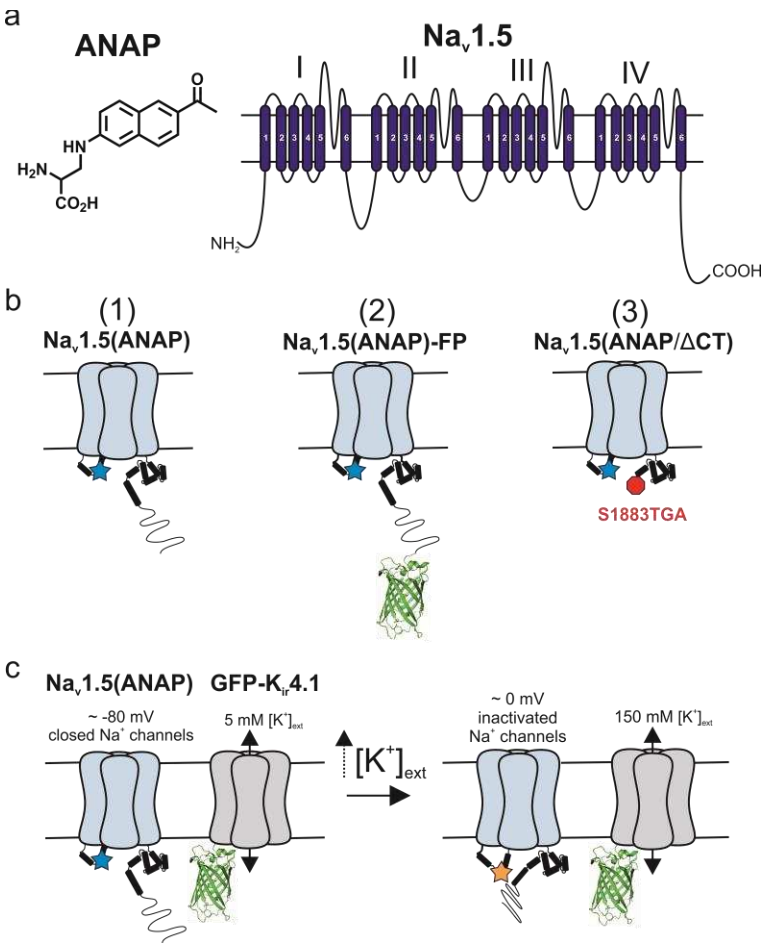

**Figure 1: $Na_v1.5$ constructs and $K^+$-depolarization assay schematic.** (a) Chemical structure of ANAP (left), $Na_v1.5$ domain structure (right). (b) $Na_v1.5$(ANAP) constructs used in imaging and electrophysiology experiments. Star=ANAP (c) Schematic of $K^+$-depolarization in cells expressing GFP-$K_{ir}4.1$ and $Na_v1.5$(ANAP). Net flux of $K^+$ is zero at both membrane potentials. 5 mM $[K^+]_{ext}$ and 150 $[K^+]_{int}$ set the equilibrium potential at ~-80 mV where $Na_v$ channels are expected to be closed. An increase to 150 mM $[K^+]_{ext}$ sets the equilibrium potential at ~0 mV where a large population of $Na_v$ channels is expected to be inactivated.

## Materials and methods

*Chemical reagents*

All reagents were purchased commercially. A 1.7 mM stock solution of ANAP (3-((6-acetylnaphthalen-2-yl)amino)-2-aminopropanoic acid trifluoroacetic acid salt) (AsisChem) was made in anhydrous dimethyl sulfoxide (Sigma-Aldrich). A 50 µM TTX (Abcam) solution was made in $ddH_2O$ from a 5 mM stock solution. Reagents were aliquoted and stored at -20°C. Chemicals for physiological solutions were purchased from Sigma-Aldrich and stored at room temperature, unless otherwise noted. Stock physiological solutions were stored at 4°C.

*Plasmids, cell lines, and molecular biology*

AnapRS-LeutRNA$_{CUA}$, pcDNA4-EGFP(Y40TAG) "pSWAN-GFP37TAG", and pCMV-*Mm*PylRS-PylT were gifts from Peter G. Schultz (33, 48). Template plasmids pH2B-EGFP and pcDNA3-SCN5A hh1c were available in-house. Template plasmid pH2B-mCherry was a gift from Robert Benezra (Addgene plasmid # 20972). HEK293T cells were available in-house. The GFP-$K_{ir}4.1$ HEK293T cell line was a gift from Christopher

Ahern. QuikChange site-directed mutagenesis (Stratagene) and/or Gibson Assembly (NEB) was performed according to the manufacturer's instructions with modifications as needed.

*Mammalian tissue culture and transfection*

HEK293T cells were grown in a medium containing Minimum Essential Medium (MEM) (Gibco) or Dulbecco's Modified Eagle Medium (DMEM) containing 4.5 g/L glucose, L-glutamine, and sodium pyruvate (Corning 10-013-CM), 10% Fetal Bovine Serum (FBS), 1% Penicillin-Streptomycin, and 2 mM GlutaMAX (Gibco) supplement at 37ºC in a humidified atmosphere of 5% $CO_2$. Transfections of all cell lines for western blot and live-cell imaging (6-well tissue-culture-treated plates for western blot, LabTek 8-well chambered coverglass tissue-culture-treated plates for imaging) were performed using Xtremegene HP (Roche) or Lipofectamine 2000 (Invitrogen) according to the manufacturer's instructions. A typical imaging experiment involved transfection of 1 µg total DNA including 0.6 µg $Na_v1.5$ reporter construct and 0.4 µg AnapRS-LeutRNA$_{CUA}$ (1.5:1 target protein to aaRS-tRNA mass ratio). Plasmids were co-transfected with reagent (3 µL reagent to 1 µg DNA) in Opti-MEM (Gibco). In +ANAP conditions, ANAP was added to the well at a final concentration of 10 µM ~30 minutes prior to adding transfection reaction. This recipe was scaled up to 2 µg total DNA for electrophysiology experiments, transfected in T25 flasks then split 24 hours later and seeded into 35 mm plates. EGFP or EGFP(Y40TAG) was co-transfected as a marker of cells to patch as needed (1:1 with $Na_v1.5$(TAG)). GFP-$K_{ir}4.1$ HEK293T were cultured in DMEM (Gibco), 10% FBS, 1% Penicillin-Streptomycin, 2 mM GlutaMAX, and Zeocin (Gibco) at 37ºC in a humidified atmosphere of 5% $CO_2$.

*Western blot*

HEK293T cells were seeded at $3x10^5$ cells per well in a 6-well tissue-culture-treated plate, transfected according to manufacturer's instructions. 1.2 µg of DNA encoding $Na_v1.5$(TAG)-EGFP, $Na_v1.5$-EGFP, EGFP(Y40TAG), or EGFP was co-transfected with 0.8 µg of AnapRS-LeutRNA$_{CUA}$ with Xtremegene (Roche) at a ratio of 3:1 in Opti-MEM (Gibco) supplemented with 2 mM GlutaMAX. 10 µM ANAP was added to the media ~30 minutes prior to adding transfection reaction. Transfected cells were cultured at 37°C, 5% $CO_2$ 36-48 hours before harvesting and lysis. Prior to lysis, cells were washed once with Tris-HCl-buffered saline (TBS), then lysed with Cell Lysis Buffer (Cell Signaling) with 1:100 proteasome inhibitor complex on ice for 5 minutes. Lysis buffer contained (mM) 20 Tris-HCl (pH 7.5), 150 NaCl, 1 $Na_2EDTA$, 1 EGTA, 1% Triton, 2.5 sodium pyrophosphate, 1 β-glycerophosphate, 1 $Na_3VO_4$, 1 µg/mL leupeptin. Cells were scraped and re-suspended in lysis buffer and incubated at 4°C for 30 minutes. Samples were centrifuged 10 minutes at 12,000xg then heated (55°C). Samples were loaded onto a 5% and 10% sodium dodecyl sulfate polyacrylamide gel electrophoresis (SDS-PAGE) gel and electrophoresed for 45 minutes at 10 mA/gel, then 90 minutes at 20 mA/gel. Protein gels were wet-transferred onto polyvinylidene difluoride (PVDF) membranes overnight at 4°C (15 V). The membranes were washed briefly with TBS then blocked with 5% w/v skim milk in 1x TBS with Tween 20 (TBS-T) for 30 minutes at room temperature. Membranes were then incubated with 1/8000 primary antibody (rabbit polyclonal anti-GFP) in (TBS-T) for 1 hour at room temperature. Membranes were washed 3x10 minutes at room temperature in TBS-T and incubated with secondary antibody (anti-rabbit horseradish peroxidase) 30 minutes at room

temperature. Membranes were washed 2x10 minutes at room temperature with TBS-T, then 1x10 minutes at room temperature with TBS, and developed using ECL Western Blot Detection Reagents (Bio-Rad). Images were taken by exposing light sensitive films at 30 seconds, 1 minute, 2 minutes, 3 minutes, and 5 minutes on a developer (Kodak) in a dark room. Membranes were stripped, stained with anti-β-tubulin, and imaged as above.

*Whole-cell patch-clamp electrophysiology*

***Sodium channel electrophysiology***

Electrophysiological recordings of sodium channels expressed in HEK293T were carried out in a whole-cell patch clamp configuration using physiological solutions. Pipette resistances ranged from 1.5-4 MOhm. The $I_{Na}$ internal solution contained (mM) 50 aspartic acid, 60 CsCl, 5 $Na_2$-ATP, 11 EGTA, 10 HEPES, 1 $CaCl_2$ and 1 $MgCl_2$, with pH 7.4 adjusted with CsOH. The $I_{Na}$ external solution contained (mM) 130 NaCl, 2 $CaCl_2$, 5 CsCl, 1.2 $MgCl_2$, 10 HEPES, 5 glucose, with pH 7.4 adjusted with CsOH. Whole cell sodium currents were recorded under voltage-clamp conditions. A voltage step protocol was used, holding at -100 mV, step depolarization to -20 mV for 200 ms, then back to holding. Cells were pulsed at a frequency of 0.1 Hz. SSI voltage protocol was as follows: holding at -100 mV or -90 mV, step to the conditioning pulse for 500 ms, depolarization to -10 mV for 20 ms, return to holding. Conditioning pulses ranged from -130 mV to -20 mV. Late sodium current was measured as TTX-sensitive current 200 ms after depolarization to -20 mV. Percent late current was measured as the average current between 195 mV and 200 mV divided by the peak current. Data was collected using an Axopatch 200B amplifier (Axon Instruments) and Digidata 1440A

digitizer. Data was recorded with pClamp8, 10, or 10.5 (Molecular Devices). Capacitive current and series resistance compensation were carried out using analog techniques according to the amplifier manufacturer (Axon Instruments). All measurements were obtained at room temperature (25°C). Statistical significance was determined using single-factor ANOVA when comparing multiple groups and Student's t-test assuming equal or unequal variances based on a prior F-test of variance. $p<0.05$ was considered statistically significant.

***Potassium channel electrophysiology***

Electrophysiological recordings of GFP-$K_{ir}$4.1 HEK293T were recorded under voltage-clamp or current-clamp conditions. Internal solution contained (mM) 150 KCl, 3 $MgCl_2$, 5 EGTA, 10 HEPES, with pH 7.4 adjusted with KOH. Extracellular solution contained (mM) 150 NaCl, 5 KCl, 1 $MgCl_2$, 1.8 $CaCl_2$, 10 HEPES, with pH 7.4 adjusted with NaOH. Changes in membrane potential were recorded over time once patch stability and $K_{ir}$4.1 channel expression were confirmed by applying a voltage ramp protocol: cells were held at -80 mV and a 500 ms voltage ramp was applied once every 3 seconds, with voltage increasing linearly from -120 mV to +60 mV, then returned to holding. Using pClamp software, a 50x data reduction of recordings was performed for data transfer compatibility to Microsoft Excel and Origin (Microcal Software) software. All measurements were obtained at room temperature (25°C). Where appropriate, as in comparing reversal potentials between low $K^+$ and high $K^+$, statistical significance was determined using Student's t-test assuming equal or unequal variances based on a prior F-test of variance. $p<0.05$ was considered statistically significant.

*Live-cell imaging*

***ANAP incorporation and spectral imaging of different sites in $Na_v1.5$***

HEK293T cells were plated at a density of 10,000-20,000 cells per well in LabTek 8-well chambered coverglass tissue-culture-treated plates (Nunc, 1.5 borosilicate) 12-24 hours before transfection. Transfections were performed as described previously. Fluorescence microscopy and spectral imaging of ANAP incorporated at different sites in $Na_v1.5$ were performed on a Zeiss LSM 700 confocal microscope (Zeiss). ANAP was excited at 405 nm and spectral emission collected from 410-600 nm in 10 nm intensity bins (Zeiss). To match the laser intensity as accurately as possible, intensity over wavelength was measured for each manually chosen ROI, normalized to ROI area, and subtracted by a laser line background area-normalized spectrum measured nearby the original ROI which did not contain a visible cell. Laser-subtracted spectra were then normalized to the sum of the intensities under the peak. Resulting normalized spectra were averaged and errors determined as ±SEM. Peak centroids of each averaged spectrum were calculated as:

$$Peak\ Centroid = \frac{sum(wavelength * intensity)}{sum(intensity)}$$

***ANAP spectral imaging with $K^+$-depolarization***

Spectral imaging for the $K^+$-depolarization experiment was performed on a Nikon A1RMP confocal microscope with spectral detector (Nikon). Cells were maintained at 37°C in a 5% $CO_2$ humidified atmosphere on the microscope with a stage-top incubator in live-cell imaging solution (MolecularProbes) or electrophysiological solutions. Live-cell imaging solution contained (mM) 140 NaCl, 2.5 KCl, 1.8 $CaCl_2$, 1.0 $MgCl_2$, 20 HEPES, with pH 7.4. In $K^+$-depolarization experiments, low $K^+$ external solution contained (mM)

150 NaCl, 5 KCl, 1 $MgCl_2$, 1.8 $CaCl_2$, 10 HEPES, with pH 7.4 adjusted with NaOH. High $K^+$ external solution contained (mM) 150 KCl, 5 NaCl, 1 $MgCl_2$, 1.8 $CaCl_2$, 10 HEPES, with pH 7.4 adjusted with KOH. During imaging, cells were maintained in low $K^+$ external solution before buffer exchange to high $K^+$. ANAP was excited at 405 nm and spectral emission collected from 402-588 nm in 6 nm intensity bins using the spectral detector. The three shortest wavelength bins were affected by a mechanical filter inside the spectral detector - a metal finger blocker just after the grating which prevents excitation light from entering the photomultiplier arrays. Unmixed ANAP or GFP spectra had negligible intensities at the affected wavelengths (Figure S2). Data analysis was performed as follows. Composite ANAP and GFP spectra were fitted and unmixed using a MATLAB (Mathworks) linear unmixing algorithm built in-house. Three spectral components were modeled to fit and unmix experimental spectra: (1) ANAP, (2) 405 nm laser line, and (3) GFP. First, the model ANAP spectrum was extracted from ANAP-only control HEK293T expressing $Na_v1.5$(Q1475ANAP) and fit as the linear combination of two gaussians to obtain a smooth spectrum. Second, a model spectrum of the peak 405 nm laser light background was determined by measuring spectra from ROIs drawn where there were no visible cells. Third, the GFP model spectrum was extracted from GFP-only control GFP-Kir4.1 co-transfected with $Na_v1.5$(Q1475TAG) and AnapRS-LeutRNA$_{CUA}$ in the absence of ANAP. The GFP model spectrum was laser-subtracted using the model spectrum of the laser light background determined in (2). The best GFP fit was a linear combination of two log-normal distributions(49). Once the model spectra were obtained, least squares regression was performed over the entire wavelength range (402-588 nm) to fit how bright each of the peaks need to be to explain the

observed spectrum at each wavelength. To account for ANAP shifts, the least squares fit was calculated at one particular wavelength of ANAP and the residual was recorded. The code iterated 20 nm to the left and right of the peak in 1 nm steps, down-sampled to the instrument resolution, until residuals were minimized, resulting in the best fit overall.

**Results**

*Fluorescent ncAA ANAP was incorporated into the $Na_v1.5$ inactivation gate in mammalian cells.*

Can fluorescent ncAA ANAP be incorporated into the human $Na_v1.5$ inactivation gate in mammalian cells? In proof-of-principle ANAP incorporation experiments, EGFP or mCherry was fused to the human $Na_v1.5$ CT as a reporter of full-length channel expression (Figure 1b, construct 2). ANAP-dependent expression of full-length $Na_v1.5$-EGFP (~275 kDa) was measured by western blot for four sites: Q1475TAG, F1485TAG, E1488TAG, and E1489TAG (Figure 2a). In the presence of ANAP, a band was observed above 200 kDa, corresponding to the more intense positive control band of the same size, representing full-length $Na_v1.5$-EGFP. The positive control for ncAA incorporation was to incorporate ANAP into EGFP(Y40TAG). ANAP-dependent full-length expression of EGFP (~27 kDa) was observed at ~50 kDa, corresponding to the band from cells expressing wild-type EGFP (Figure 2a). In both cases, no band was observed in the absence of ANAP. β-tubulin normalized band intensities in the ncAA incorporation conditions were 16% for Q1475ANAP, 7% for F1485ANAP, 11% for E1488ANAP, and 31% for E1489ANAP, of that in the wild-type condition. These results demonstrate ANAP-dependent expression of full-length sodium channel reporter protein

in mammalian cells and emphasize the high variability in ncAA-incorporation efficiency depending on target incorporation site.

$Na_v1.5$ was tested for permissibility to ANAP incorporation. A site in DIII:S6 Q1475TAG was chosen initially for ANAP incorporation because we hypothesized that this site being close to the membrane-cytosol interface would elicit detectable spectral shifts representing changes in hydrophobicity in the $K^+$-depolarization assay (26, 30). HEK293T cells expressing $Na_v1.5$(Q1475ANAP)-mCherry were imaged by confocal microscopy (Figure 2b). In the +ANAP condition, ANAP and mCherry fluorescence was observed at the plasma membrane and localized to intracellular compartments (Figure 2b, columns 1,2). This was expected due to the absence of β subunit overexpression, which can cause defective plasma membrane trafficking (50). ANAP fluorescence intensity correlated ($R^2$=0.6) with mCherry fluorescence intensity in the $Na_v1.5$(Q1475ANAP)-mCherry condition (Figure 2c, right). As a negative control representing background ANAP fluorescence, wild-type $Na_v1.5$-mCherry and AnapRS-LeutRNA$_{CUA}$ were co-expressed in HEK293T+10 μM ANAP (Figure 2b, column 3). Bright mCherry fluorescence and dim ANAP fluorescence was observed, but ANAP signal was significantly decreased compared to the $Na_v1.5$(Q1475ANAP)-mCherry condition (Figure 2c, left).

As a negative control to evaluate ANAP-independent expression of the reporter protein, $Na_v1.5$(Q1475TAG)-mCherry was expressed in the presence of AnapRS-LeutRNA$_{CUA}$ in HEK293T grown without ANAP (Figure 2b, column 4). Cell auto-fluorescence and dim mCherry signal were observed, but both signals were decreased compared to the $Na_v1.5$(Q1475ANAP)-mCherry condition. Together, these data

demonstrated ANAP-dependent full-length $Na_v1.5$ expression, suggesting that ANAP can be incorporated into the inactivation gate. Furthermore, ANAP fluorescence signal can be visualized and distinguished from background by routine confocal imaging.

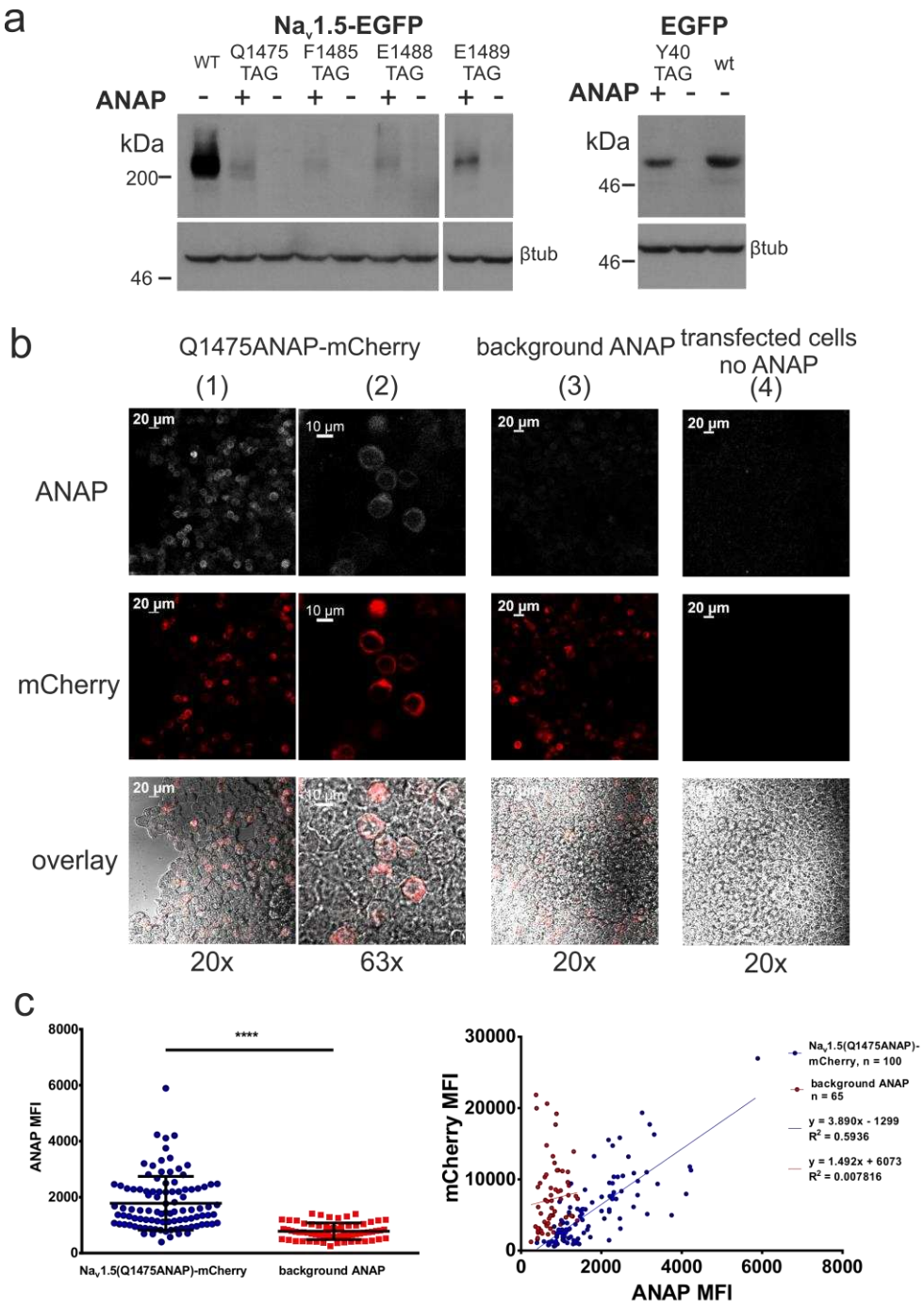

**Figure 2: Full-length $Na_v1.5$ expression depends on presence of ANAP and its synthetase-tRNA pair.** (a) Western blot of $Na_v1.5$(Q1475TAG)-EGFP and EGFP(Y40TAG) grown in HEK293T ±10 μM ANAP, probed with rabbit pAb-GFP. All conditions were co-transfected with AnapRS-tRNALeu$_{CUA}$. (Left) $Na_v1.5$-EGFP, 5% SDS-PAGE, 5 min exposure. (Right) EGFP, 10% SDS-PAGE, 1 min exposure. Each image in its entirety was adjusted for contrast and brightness enhancement. Full-length EGFP is ~27 kDa and was observed ~50 kDa in this blot. Full-length $Na_v1.5$-EGFP is ~275 kDa and was observed above 200 kDa in this blot. (b) Fluorescence imaging of HEK293T expressing $Na_v1.5$(Q1475ANAP)-mCherry (columns 1, 2), $Na_v1.5$-mCherry+10 μM ANAP (background ANAP, column 3), or $Na_v1.5$(Q1475TAG)-mCherry in the absence of ANAP (transfected cells no ANAP, column 4). ANAP (ex405, em445/50 nm) and mCherry (ex555, em647/70 nm) fluorescence were imaged. Overlay image includes ANAP (white), mCherry (red), and brightfield channels. All except brightfield images were equally adjusted in their entirety for contrast enhancement. (c) Quantification of the 20x images in (b). (Left) ANAP mean fluorescence intensity (MFI) was significantly increased when the target codon for incorporation was present. ****$p<0.0001$, two-tailed unpaired t-test with Welch's correction. (Right) mCherry MFI plotted as a function of ANAP MFI.

*Electrophysiology of ANAP incorporated full-length and ΔCT truncated $Na_v1.5$ in cells.* We asked whether functional channel expression at the plasma membrane depended on the presence of ANAP and its incorporation machinery. Furthermore, because the $Na_v1.5$ inactivated state is stabilized by helix 6 in the CT structured region, we sought to measure the effect of truncating helix 6 and the entire distal CT on $Na_v1.5$(ANAP)

function (8, 20–23). We used the previously characterized truncation mutation S1883TGA (ΔCT) (8). Patch-clamp electrophysiology was used to characterize $Na_v1.5$(Q1475ANAP), $Na_v1.5$(ΔCT), or $Na_v1.5$(Q1475ANAP/ΔCT) co-expressed with EGFP(Y40ANAP) in HEK293T cells. EGFP(Y40ANAP) was a marker of cells able to carry out ncAA incorporation. In +ANAP conditions, TTX-sensitive sodium currents were observed in EGFP-positive cells (Figure 3a), although peak current density was significantly decreased compared to wild-type channels (Figure 3b). Decreased peak current density of ANAP incorporated channels could be due to defects in channel trafficking to the plasma membrane, lower channel expression, or a decrease in single channel conductance. Notably, small or no currents were observed in cells expressing all components for ANAP incorporation but grown in the absence of ANAP (Figure 3a,b). This suggests that sodium currents observed in the presence of ANAP are dependent on ANAP incorporation and represent full-length $Na_v1.5$(Q1475ANAP) or truncated $Na_v1.5$(Q1475ANAP/ΔCT) channels.

Next, the inactivation properties of $Na_v1.5$(Q1475ANAP) and $Na_v1.5$(Q1475ANAP/ΔCT) channels were characterized. Macroscopically, currents resembled $Na_v$ channels, with rapid opening and inactivation in response to a step change in membrane depolarization. There was lengthened time to half-complete inactivation ($t_{1/2}$) and increased late current ($I_{Na,L}$) in cells expressing $Na_v1.5$(Q1475ANAP), $Na_v1.5$(ΔCT), or $Na_v1.5$(Q1475ANAP/ΔCT) (Figure 3d,e). The steady-state inactivation (SSI) curve of $Na_v1.5$(Q1475ANAP), a measure of voltage-dependent transitions between the closed and closed-inactivated states, was shifted towards more depolarized potentials relative to wild-type, suggesting destabilized

inactivation and thus, an increase in availability of these channels to open and inactivate (Figure 3c). The SSI curve of $Na_v1.5$(ΔCT) was shifted towards hyperpolarized potentials relative to wild-type (Figure 3c). Incorporation of ANAP at Q1475 resulted in a depolarizing shift of the SSI curve relative to wild-type, and the combination of Q1475ANAP/ΔCT counteracted the depolarizing shift (Figure 3c). Together, electrophysiological data suggest that ANAP can be incorporated at Q1475 in the $Na_v1.5$ inactivation gate to make functional channels. While channel function is different from wild-type, it is within pathophysiological range (51–53).

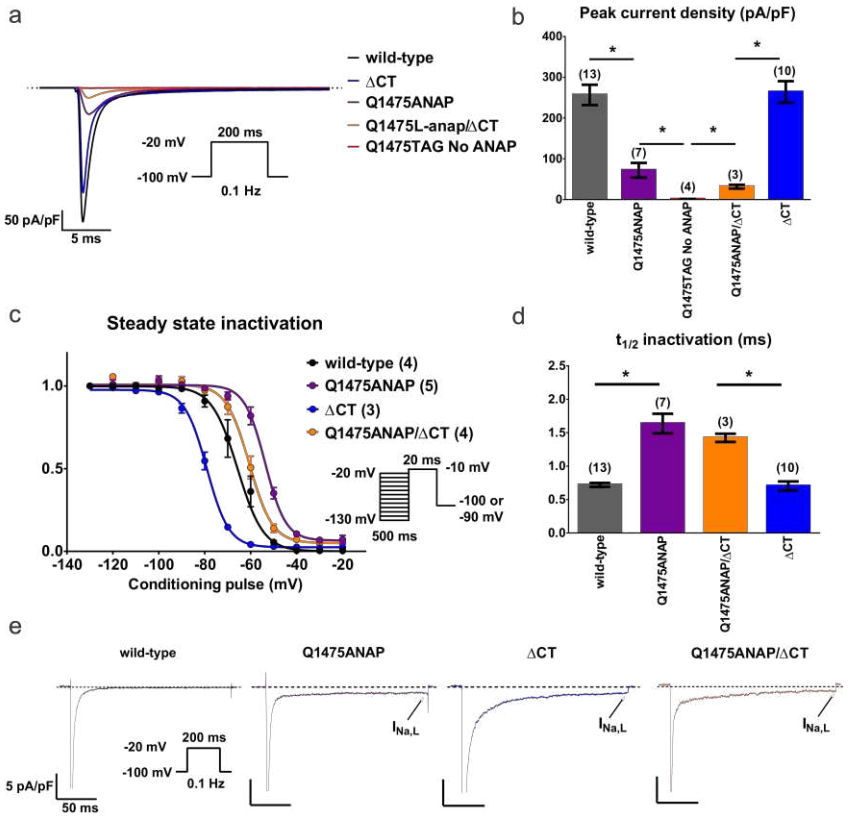


**Figure 3: Electrophysiology of ANAP incorporated full-length and ΔCT truncated $Na_v1.5$ in HEK293T cells.** (a) Representative TTX-sensitive capacitance-normalized current traces of wild-type $Na_v1.5$, $Na_v1.5$(ΔCT), $Na_v1.5$(Q1475ANAP), or

$Na_v1.5$(Q1475ANAP/ΔCT) expressed in HEK293T. All conditions were co-transfected with AnapRS-LeutRNA$_{CUA}$. Inset is the voltage protocol. (b) Average peak current density (pA/pF) of all conditions. Numbers above bars are the number of cells *(left to right) two-tailed p=$8.5x10^{-5}$, $1.7x10^{-5}$, 0.02, $5.6x10^{-6}$, Student's t-test. Peak currents and cell capacitances are in Figure S1. (c) Steady state inactivation of all constructs ±10 μM ANAP. Inset is the voltage protocol. Numbers in legend refer to number of cells. $V_{1/2}$: WT -64.6±0.4 mV, Q1475ANAP -51.8±0.7 mV, ΔCT -79.2±0.4 mV, Q1475ANAP/ΔCT -59.7±0.6 mV (d) Time to half-complete inactivation ($t_{1/2}$, ms) of all constructs. Numbers above bars are the number of cells. *(left to right) two-tailed p=0.0009, 0.0002, Student's t-test. (e) High-gain TTX-sensitive capacitance-normalized traces of all constructs using same voltage protocol as in (a). Arrow indicates late sodium current ($I_{Na,L}$). $I_{Na,L}$ (% peak current, late current density): WT (0.3%, 1 pA/pF), Q1475ANAP (1.3%, 0.9 pA/pF), ΔCT (0.46%,1.2 pA/pF), Q1475ANAP/ΔCT (3.1%, 0.8 pA/pF).

*Spectral imaging of $Na_v1.5$ANAP enables sensing of hydrophobicity in intracellular environment.*

We then asked if ANAP environmentally sensitive fluorescence could be measured in mammalian cells. Spectral imaging was used to measure ANAP fluorescence emission and spectral shifts in mammalian cells. Four different sites were tested for ANAP incorporation into $Na_v1.5$(TAG) expressed in HEK293T (Figure 4a). ANAP spectra associated with each site demonstrated unique emission peaks: $Na_v1.5$(Q1475ANAP) (centroid 480 nm), $Na_v1.5$(F1485ANAP) (centroid 484 nm), $Na_v1.5$(E1488ANAP) (centroid 482 nm), and $Na_v1.5$(E1489ANAP) (centroid 483 nm) (Figure 4b). Background

ANAP in the presence of wild-type $Na_v1.5$ was red-shifted with a peak centroid of 489 nm. The fluorescence ratio F456nm/F499nm was significantly different between sites, with $Na_v1.5$(Q1475ANAP) being the most blue-shifted (high F456nm/F499nm) and F1485ANAP (low F456nm/F499nm) the most red-shifted (Figure 4c). As a test for the reliability of observations using spectral imaging and separation of signal spectrum from laser light, results were compared between biological replicates and the resulting shifts were not significantly different (Figure S3). A blue-shift represents a more hydrophobic environment. Thus, $Na_v1.5$(Q1475ANAP) was situated in the most hydrophobic environment; the location of this site at the end of DIII-S6 lends itself to an expectation of a more hydrophobic environment (26, 30). $Na_v1.5$(F1485ANAP) was in a relatively less hydrophobic environment. Background ANAP was red-shifted and therefore was situated in the least hydrophobic environment. These data represent sensing of hydrophobicity in the local environment of ANAP incorporated in the inactivation gate of full-length $Na_v1.5$ expressed in mammalian cells.

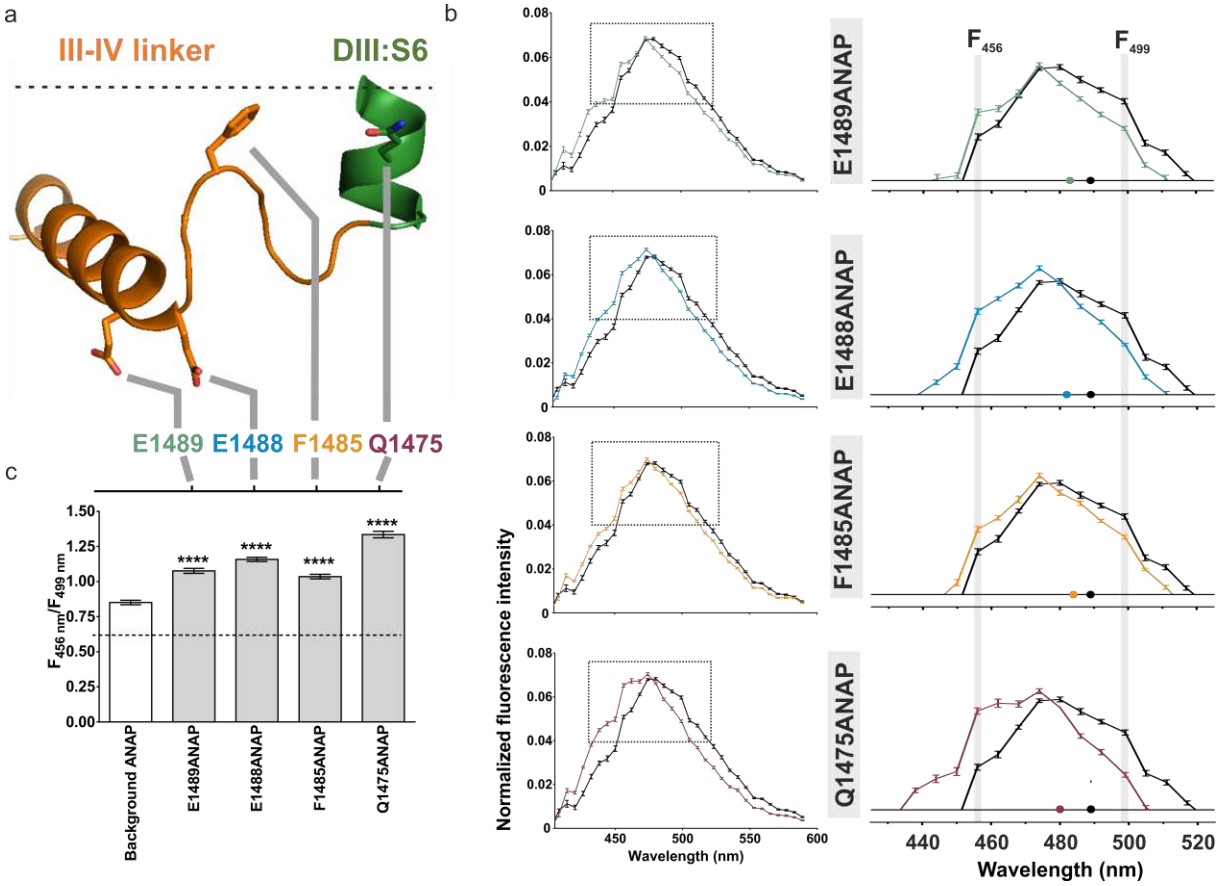


**Figure 4: ANAP spectral imaging afforded detection of hydrophobicity in intracellular environment.** (a) Schematic of the inactivation gate depicting the location of the four sites tested, Q1475, F1485, E1488, and E1489. F1485 is a part of the IFM motif, known as the inactivation particle. Approximate location of the membrane is depicted by the dashed line. Adapted from PDB structure 5XSY (27) (b) ANAP spectra, laser line background subtracted and normalized to the sum of intensities under each peak. ANAP at each of the four sites is compared with background ANAP control (wild-type $Na_v1.5$+10 μM ANAP, black). Dashed box shows inset where spectra are zoomed in on the peak. n=12 cells for each condition, representative of 2 experiments, error bars

are ±SEM. (c) Fluorescence ratio $F_{456nm}/F_{499nm}$ measured for each condition, error bars are ±SEM. ****p < 0.0001, ANOVA with Tukey's multiple comparisons test.

*A spectral imaging assay allows measurement of $Na_v1.5$ conformational change in mammalian cells.*

A spectral imaging assay was developed to detect ANAP fluorescence changes correlated with inactivated states of $Na_v1.5$ channels expressed in mammalian cells. Q1475ANAP was chosen as a proof-of-principle for the spectral imaging assay because we hypothesized that this site being close to the membrane-cytosol interface would elicit detectable spectral shifts representing changes in hydrophobicity. We explored the effect of the ΔCT mutation on ANAP spectra with $K^+$-depolarization since truncation of the distal CT destabilizes the inactivated state, causing a marked shift in the voltage-dependence of SSI (8, 23). We hypothesized that these changes would cause a conformational change that ANAP fluorescence shifting would reflect.

Spectral imaging of ANAP was combined with $K^+$-depolarization such that sodium channel state could be changed from closed to inactivated during imaging. In order to control membrane potential without voltage clamp we used $K_{ir}4.1$, which is sensitive to $[K^+]_{ext}$ and thus enables (1) establishment of the initial RMP at a hyperpolarized potential such that VGSCs will be closed and available, and (2) steady state depolarization of the RMP upon addition of increased $[K^+]_{ext}$ to drive the transition between VGSC closed and inactivated states (54–56). Based on SSI curves of $Na_v1.5$(Q1475ANAP) (Figure 3c), when the resting membrane potential (RMP) is set to a hyperpolarized potential, channels at the membrane are expected to be in the resting, closed-available state (Figure 1c). With a depolarization of the membrane, channels are

expected to open and quickly inactivate, or undergo transitions to slow-inactivated and/or closed-inactivated states, resulting in a mixed population of inactivated channels at steady state (Figure 1c) (57).

A stable HEK293T cell line expressing GFP-$K_{ir}$4.1 was obtained to control RMP during spectral imaging experiments. A representative current-clamp trace demonstrates that transition from 5 mM $[K^+]_{ext}$ (low $K^+$) to 150 mM $[K^+]_{ext}$ (high $K^+$) changed the membrane potential from -76 mV to -5 mV (Figure 5a, left). The reversal potential of these cells was shifted from approximately -80 mV to 0 mV with increased $[K^+]_{ext}$ (Figure 5a, right). Expression of $Na_v$1.5(ANAP) in the GFP-$K_{ir}$4.1 HEK293T cell line resulted in composite ANAP-GFP spectra that were unmixed and fitted to measure shifting ANAP peaks (Figure S4). Dual-fluorescent ANAP- and GFP-positive cells were manually chosen for spectral analysis. The spectrum from each cell was individually unmixed from laser line background and GFP.

To enhance the reliability of unmixing of spectra and to isolate cells expressing GFP-$K_{ir}$4.1, selection criteria were introduced in post-processing. First, as a goodness-of-fit measure, the summed absolute residuals (SAR) after the fit were compared to the total intensity (TI) in the spectrum. A threshold in the SAR-TI ratio was identified empirically as one at which the standard deviation of the shift in the fitted ANAP peak rapidly started to increase (Figure S6a). Cells with SAR/TI<0.04 were excluded from further processing. Second, spectra from reliably expressing GFP-$K_{ir}$4.1 cells were selected by comparing the amplitude of the fitted GFP peak (AGFP) to the SAR. The AGFP-SAR ratio below which the GFP signal was comparable to the residuals was deemed the threshold for accepting a positive identification of GFP-$K_{ir}$4.1 expression, at

AGFP/SAR>0.3 (Figure S6b, c). Since certain spectra showed high expression of GFP with relatively low ANAP signals, a further criterion was introduced to ensure that a well resolved ANAP signal existed - ANAP amplitude (AA) to SAR ratio above AA/SAR>1.

Spectra of $Na_v1.5$(Q1475ANAP) show ANAP fluorescence shifts depending on $[K^+]_{ext}$ and presence of the distal CT (Figure 5b). GFP peaks were unaltered in the same experiments (Figure S5). $K^+$-depolarization caused a small but significant red-shift in the ANAP spectra of full-length $Na_v1.5$(Q1475ANAP) (Figure 5b, left). Notably, $K^+$-depolarization caused no change in ANAP spectra of ΔCT channels (Figure 5b, center). The red-shift was not observed in cells expressing $Na_v1.5$(Q1475ANAP) but failing the GFP threshold test, validating that the spectral shift depends on the presence of GFP-$K_{ir}1.4$ and thus on the membrane potential (Figure 5b, right). These data suggest the distal CT plays a role in mediating inactivation gate conformational change associated with inactivation. A general ANAP spectral imaging $K^+$-depolarization assay for probing $Na_v1.5$ conformational change in channels expressed in mammalian cells has been established.

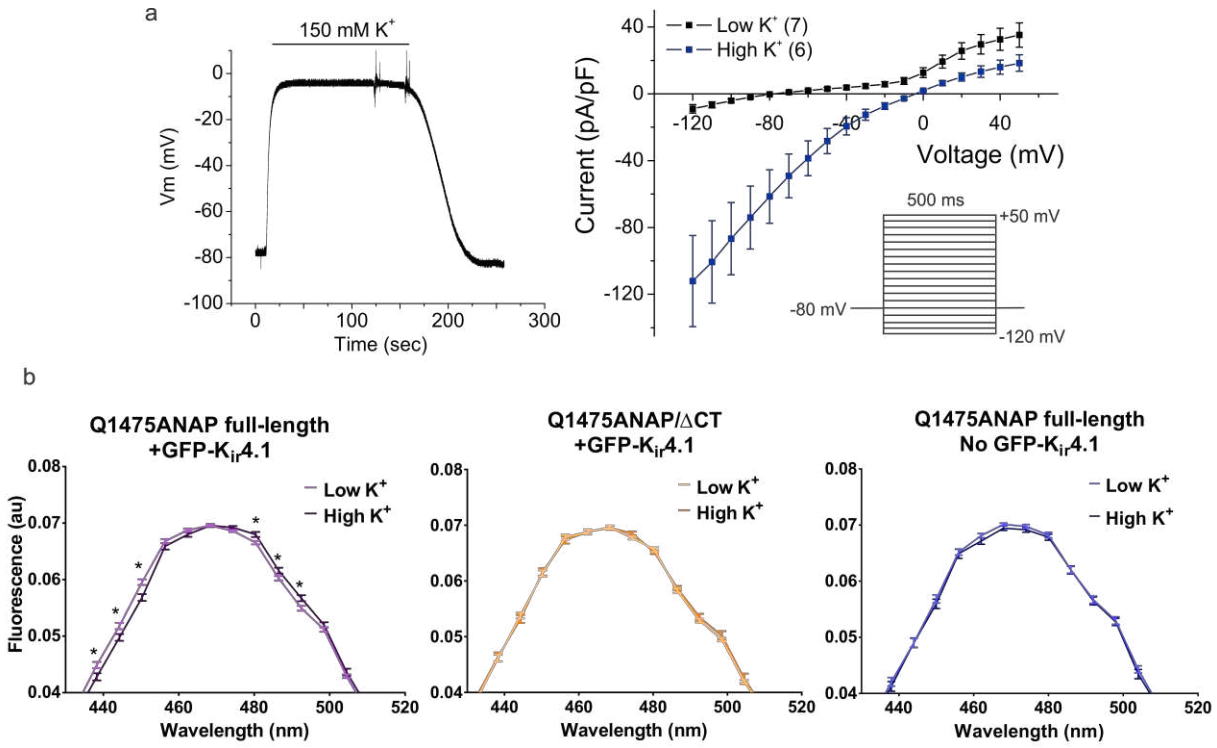


**Figure 5: A $K^+$-depolarization ANAP spectral imaging assay of $Na_v1.5$ conformational change.** (a) Establishment of $K^+$-depolarization to control resting membrane potential (RMP). (left) Representative current-clamp trace of GFP-$K_{ir}$4.1 HEK293T stable cells. Range in $V_m$ is -80 mV to 0 mV with increasing $[K^+]_{ext}$ from 5 mM to 150 mM. (right) Reversal potential of GFP-$K_{ir}$4.1 cells can be changed from -80 mV in low $K^+$ (5 mM $[K^+]_{ext}$) to ~0 mV in High $K^+$ (150 mM $[K^+]_{ext}$). Inset is the voltage protocol. (b) Spectra of full-length $Na_v1.5$(Q1475ANAP) (left) and $Na_v1.5$(Q1475ANAP/ΔCT) (middle) in cells expressing GFP-$K_{ir}$4.1 and $Na_v1.5$(Q1475ANAP) in cells with no GFP-$K_{ir}$4.1 (AGFP/SAR<0.3) (right), at low $K^+$ and high $K^+$. Q1475ANAP low $K^+$, n=36 cells, Q1475ANAP high $K^+$, n=30 cells, Q1475ANAP/ΔCT low $K^+$, n=21 cells, Q1475ANAP/ΔCT high $K^+$, n=19 cells, Q1475ANAP no GFP-$K_{ir}$4.1 low $K^+$, n=18 cells, Q1475ANAP no GFP-$K_{ir}$4.1 high $K^+$, n=16 cells. Error bars are ± standard error of the average relative brightness of the channel. Spectra are zoomed in on the peak. *p

values (left to right) full-length $Na_v1.5$(Q1475ANAP): p=0.02, 0.02, 0.0009, 0.008, 0.04, 0.01, Student's t-test.

**Discussion**

Site-specific incorporation of the environmentally sensitive fluorescent ncAA ANAP into the $Na_v1.5$ intracellular inactivation gate was achieved using synthetase-tRNA technology in mammalian cells. ANAP incorporated into a fluorescent reporter $Na_v1.5$(Q1475TAG)-mCherry was imaged, demonstrating ANAP and mCherry fluorescence localization at the cell membrane and intracellular compartments (Figure 2b). In $Na_v1.5$(Q1475ANAP)-mCherry imaging experiments, ANAP background fluorescence was observed and may result from incomplete washout of unincorporated ANAP. Also, ANAP incorporation could potentially occur at non-target amber codons. In the absence of ANAP, auto-fluorescence was observed in the ANAP channel and dim mCherry fluorescence was observed in the mCherry channel. Collected ANAP emission was in the blue visible light spectrum where auto-fluorescence is expected due to natural amino acids and other biomolecules such as NADH and NADPH (58, 59). mCherry background fluorescence may result from ANAP-independent readthrough of the target stop codon or initiation of mCherry expression. It is notable that auto-fluorescence and background mCherry fluorescence signals were negligible compared to fluorescence signals when ANAP and its target site of incorporation were present (Figure 2b,c).

Patch-clamp electrophysiology revealed ncAA-dependent sodium currents in cells expressing $Na_v1.5$(Q1475ANAP) or $Na_v1.5$(Q1475ANAP/ΔCT), whereas little to no sodium currents were observed in the absence of ANAP (Figure 3), further

corroborating successful incorporation of the fluorescent ncAA ANAP into functional channels. Electrophysiological characterization of $Na_v1.5$(Q1475ANAP) and $Na_v1.5$(Q1475ANAP/ΔCT) demonstrated decreased peak current density, and for ANAP incorporation, imaging data suggest a considerable population of fluorescent channels was localized in intracellular compartments (Figure 2b). Decreased peak current density could represent defective channel trafficking, lower channel expression, or decreased single-channel conductance. Single-channel functional characterization was not performed in this work and would clarify the possible effect of each ncAA on single-channel conductance. However, defective trafficking and lower channel expression are expected to be primary causes of decreased peak current density. Lower expression of ncAA-incorporated channels is expected due to competition with endogenous release factors at the site of incorporation (31). Defects in channel trafficking to the membrane are known to occur in the absence of β subunit overexpression, and could be compounded by an unknown trafficking effect associated with ncAA-incorporated channels (50); co-expression with β subunit would likely improve $Na_v1.5$(ANAP) expression at the membrane and should be employed in future work. Single amino acid mutation of this region is sufficient to alter channel function, evidenced by LQT3 mutations and the work herein (51). While channel function was altered by ANAP incorporation into the inactivation gate, properties remained within pathophysiological range, and most closely mimicked those of a characterized LQT3 mutant channel F1473C (51). The method developed herein facilitates experiments with LQT3 mutant channels that could elucidate $Na_v1.5$ structural dynamics in a pathological context.

Spectral imaging was used to measure ANAP emission in $Na_v1.5$ in live mammalian cells. Unique ANAP spectra were observed with ANAP incorporated at four different sites in $Na_v1.5$ Q1475, F1485, E1488 and E1489, and spectra were red-shifted in the absence of a target stop codon for incorporation, indicating sensing of hydrophobicity in local environment of the inactivation gate (Figure 4). It should be noted that fluorescence from background ANAP (unincorporated or in a channel not in the membrane) cannot be separated from target-incorporated ANAP fluorescence at this point. Therefore, the interpretation of absolute shifts in ANAP spectra cannot be clear, and we restrict our conclusions to relative shifts. While imaging data suggest a considerable portion of ANAP was localized to intracellular compartments, electrophysiology data showed that a detectable population of functional channels reached the plasma membrane in an ANAP-dependent fashion. Spectra from the membrane only vs. membrane and cytosol exhibited no observable difference in our setup, so spectra from the whole cell were analyzed to maximize ANAP signal (Figure S2).

This study provided proof-of-principle evidence of a $K^+$-depolarization ANAP spectral imaging assay which was developed to detect effects on conformational rearrangement of the inactivation gate in response to a change in membrane potential without patch-clamp. For this purpose, experiments were performed to test the specific effects of the ΔCT and channel state. $K^+$-depolarization allowed sodium channel state at the plasma membrane to be changed from closed to a mixture of open- and closed-inactivated states in a steady-state fashion during spectral imaging (Figure 1c). The timescale of the $K^+$-depolarization assay was significantly longer than that of fast

inactivation, therefore it is more likely the assay detected intermediate- or slow-inactivated states (57). When channels are inactivated and the CT is intact, a change in the position of DIII-S6 (relative to resting) may increase hydrophobicity in the environment of Q1475ANAP leading to a subtle red-shift in the ANAP spectra (Figure 5b, left). The change in position of DIII-S6 may lead to a change in the affinity of the III-IV linker-pore complex, destabilizing the inactivation gate. ANAP spectra were unshifted in ΔCT channels with K-depolarization, which may suggest that the absence of the distal CT can prevent entry into inactivated states, although it is possible there is a conformational change that is undetectable with the current experimental setup.

Simultaneous electrophysiology and fluorescence measurements in mammalian cells would definitively link ANAP spectral shifts to $Na_v1.5$ inactivation dynamics and characterization of all the ANAP-incorporated sites in the $K^+$-depolarization assay would further validate the method. The ability to label the inactivation gate and measure fluorescence spectral shifts associated with VGSC conformational change is an invaluable method setting the foundation for such future studies. Notably, the presented method could be used to screen environmentally sensitive positions in $Na_v1.5$ or other channels in mammalian cells as a first-pass substitute for patch-clamp fluorometry.

**Conclusion**

ANAP was incorporated into the $Na_v1.5$ inactivation gate in mammalian cells, resulting channel function was modestly perturbed, and ANAP fluorescence was sensitive to the intracellular environment, as well as to channel state. Site-specific fluorescent incorporation of ANAP combined with $K^+$-depolarization enabled direct monitoring of $Na_v1.5$ inactivation gate conformational rearrangement in channels expressed in live

mammalian cells. The $K^+$-depolarization ANAP spectral assay is a general assay for studying conformational dynamics of the $Na_v1.5$ inactivation gate and regulators thereof in mammalian cells. It could provide insight on outstanding questions of VGSC regulation, for instance, by calcium, kinases (PKA, CAMKII, Fyn), and growth factors (FHF) (60). Furthermore, the development of such an assay can similarly be applied to other ion channels and membrane proteins to gain site-specific knowledge of their conformational dynamics in mammalian cells.

**Author contributions**

MAS, VWC, and RSK devised the project. MAS designed and performed experiments and wrote the manuscript. JRQ contributed to experimental design and performed experiments. MY contributed to experimental design. VWC and RSK designed experiments and supervised research. All authors reviewed the final results and edited the manuscript.

**Acknowledgements**

MAS was supported by a Columbia University Research Initiatives in Science and Engineering Award. We thank Istvan Cziegler for assistance with imaging data analysis, Cecile Terrenoire and Seth Robey for assistance with electrophysiology experiments, Kevin Sampson and Manu Ben-Johny for assistance with the manuscript, and Zhixing Chen, Casey Brown, and Chaoran Jing for insightful conversations. We thank Christopher Ahern for the GFP-$K_{ir}4.1$ stable cell line. We thank Jenny Rao for technical assistance. Images were collected in the Confocal and Specialized Microscopy Shared Resource of the Herbert Irving Comprehensive Cancer Center at Columbia University,

supported by NIH grant #P30 CA013696 (National Cancer Institute). The confocal microscope was purchased with NIH grant #S10 RR025686.

**References**

1. Catterall, W.A. 2000. From Ionic Currents to Molecular Mechanisms: The Structure and Function of Voltage-Gated Sodium Channels. Neuron. 26: 13–25.

2. Kellenberger, S., J.W. West, W.A. Catterall, and T. Scheuer. 1997. Molecular analysis of potential hinge residues in the inactivation gate of brain type IIA Na+ channels. J. Gen. Physiol. 109: 607–617.

3. Kellenberger, S., J.W. West, T. Scheuer, and W.A. Catterall. 1997. Molecular Analysis of the Putative Inactivation Particle in the Inactivation Gate of Brain Type IIA Na+ Channels. J. Gen. Physiol. 109: 589–605.

4. Kellenberger, S., T. Scheuer, and W.A. Catterall. 1996. Movement of the Na+ Channel Inactivation Gate during Inactivation. J. Biol. Chem. 271: 30971–30979.

5. Smith, M.R., and A.L. Goldin. 1997. Interaction between the sodium channel inactivation linker and domain III S4-S5. Biophys. J. 73: 1885–1895.

6. West, J.W., D.E. Patton, T. Scheuer, Y. Wang, A.L. Goldin, and W.A. Catterall. 1992. A cluster of hydrophobic amino acid residues required for fast Na+-channel inactivation. Proc. Natl. Acad. Sci. 89: 10910–10914.

7. Eaholtz, G., T. Scheuer, and W.A. Catterall. 1994. Restoration of Inactivation and Block of Open Sodium Channels by an Inactivation Gate Peptide. Neuron. 12: 1041–1048.

8. Motoike, H.K., H. Liu, I.W. Glaaser, A.-S. Yang, M. Tateyama, and R.S. Kass. 2004. The Na+ Channel Inactivation Gate Is a Molecular Complex: A Novel Role of the COOH-terminal Domain. J. Gen. Physiol. 123: 155–165.

9. McPhee, J.C., D.S. Ragsdale, T. Scheuer, and W.A. Catterall. 1995. A Critical Role for Transmembrane Segment IVS6 of the Sodium Channel α Subunit in Fast Inactivation. J. Biol. Chem. 270: 12025–12034.

10. Lerche, H., W. Peter, R. Fleischhauer, U. Pika-Hartlaub, T. Malina, N. Mitrovic, and F. Lehmann-Horn. 1997. Role in fast inactivation of the IV/S4–S5 loop of the human muscle Na+ channel probed by cysteine mutagenesis. J. Physiol. 505: 345–352.

11. Filatov, G.N., T.P. Nguyen, S.D. Kraner, and R.L. Barchi. 1998. Inactivation and Secondary Structure in the D4/S4-5 Region of the SkM1 Sodium Channel. J. Gen. Physiol. 111: 703–715.

12. McPhee, J.C., D.S. Ragsdale, T. Scheuer, and W.A. Catterall. 1998. A Critical Role for the S4-S5 Intracellular Loop in Domain IV of the Sodium Channel α-Subunit in Fast Inactivation. J. Biol. Chem. 273: 1121–1129.

13. Tang, L., N. Chehab, S.J. Wieland, and R.G. Kallen. 1998. Glutamine substitution at alanine1649 in the S4-S5 cytoplasmic loop of domain 4 removes the voltage sensitivity of fast inactivation in the human heart sodium channel. J. Gen. Physiol. 111: 639–52.

14. Veldkamp, M.W., P.C. Viswanathan, C. Bezzina, A. Baartscheer, A.A.M. Wilde, and J.R. Balser. 2000. Two Distinct Congenital Arrhythmias Evoked by a Multidysfunctional Na+ Channel. Circ. Res. 86: e91–e97.

15. Bezzina, C., M.W. Veldkamp, M.P. van den Berg, A.V. Postma, M.B. Rook, J.-W. Viersma, I.M. van Langen, G. Tan-Sindhunata, M.T.E. Bink-Boelkens, A.H. van der Hout, M.M.A.M. Mannens, and A.A.M. Wilde. 1999. A Single Na+ Channel Mutation Causing Both Long-QT and Brugada Syndromes. Circ. Res. 85: 1206–1213.

16. Rivolta, I. 2001. Inherited Brugada and Long QT-3 Syndrome Mutations of a Single Residue of the Cardiac Sodium Channel Confer Distinct Channel and Clinical Phenotypes. J. Biol. Chem. 276: 30623–30630.

17. An, R.H., X.L. Wang, B. Kerem, J. Benhorin, A. Medina, M. Goldmit, and R.S. Kass. 1998. Novel LQT-3 mutation affects Na+ channel activity through interactions between α-and β1-subunits. Circ. Res. 83: 141–146.

18. Tateyama, M., H. Liu, A.-S. Yang, J.W. Cormier, and R.S. Kass. 2004. Structural Effects of an LQT-3 Mutation on Heart Na+ Channel Gating. Biophys. J. 86: 1843–1851.

19. Mantegazza, M., F.H. Yu, W.A. Catterall, and T. Scheuer. 2001. Role of the C-terminal domain in inactivation of brain and cardiac sodium channels. Proc. Natl. Acad. Sci. U. S. A. 98: 15348–15353.

20. Glaaser, I.W., J.R. Bankston, H. Liu, M. Tateyama, and R.S. Kass. 2006. A Carboxyl-terminal Hydrophobic Interface Is Critical to Sodium Channel Function: Relevance to Inherited Disorders. J. Biol. Chem. 281: 24015–24023.

21. Glaaser, I.W., J.D. Osteen, A. Puckerin, K.J. Sampson, X. Jin, and R.S. Kass. 2012. Perturbation of sodium channel structure by an inherited Long QT Syndrome mutation. Nat. Commun. 3: 706.

22. Bankston, J.R., K.J. Sampson, S. Kateriya, I.W. Glaaser, D.L. Malito, W.K. Chung, and R.S. Kass. 2007. A novel LQT-3 mutation disrupts an inactivation gate complex with distinct rate-dependent phenotypic consequences. Channels. 1: 273–280.

23. Cormier, J.W., I. Rivolta, M. Tateyama, A.-S. Yang, and R.S. Kass. 2002. Secondary Structure of the Human Cardiac Na+ Channel C Terminus: Evidence for a Role of Helical Structures in Modulation of Channel Inactivation. J. Biol. Chem. 277: 9233–9241.

24. Sarhan, M.F., C.-C. Tung, F. Van Petegem, and C.A. Ahern. 2012. Crystallographic basis for calcium regulation of sodium channels. Proc. Natl. Acad. Sci. 109: 3558–3563.

25. Wang, C., B.C. Chung, H. Yan, S.-Y. Lee, and G.S. Pitt. 2012. Crystal Structure of the Ternary Complex of a NaV C-Terminal Domain, a Fibroblast Growth Factor Homologous Factor, and Calmodulin. Structure. 20: 1167–1176.

26. Shen, H., Q. Zhou, X. Pan, Z. Li, J. Wu, and N. Yan. 2017. Structure of a eukaryotic voltage-gated sodium channel at near-atomic resolution. Science. 355: eaal4326.

27. Yan, Z., Q. Zhou, L. Wang, J. Wu, Y. Zhao, G. Huang, W. Peng, H. Shen, J. Lei, and N. Yan. 2017. Structure of the Nav1.4-β1 Complex from Electric Eel. Cell. 170: 470-482.e11.

28. Shen, H., D. Liu, K. Wu, J. Lei, and N. Yan. 2019. Structures of human Nav1.7 channel in complex with auxiliary subunits and animal toxins. Science. 363: 1303–1308.

29. Pan, X., Z. Li, X. Huang, G. Huang, S. Gao, H. Shen, L. Liu, J. Lei, and N. Yan. 2019. Molecular basis for pore blockade of human Na+ channel Nav1.2 by the m-conotoxin KIIIA. Science. 363: 1309–1313.

30. Clairfeuille, T., A. Cloake, D.T. Infield, J.P. Llongueras, C.P. Arthur, Z.R. Li, Y. Jian, M.-F. Martin-Eauclaire, P.E. Bougis, C. Ciferri, C.A. Ahern, F. Bosmans, D.H. Hackos, A. Rohou, and J. Payandeh. 2019. Structural basis of α-scorpion toxin action on Nav channels. Science. 363: eaav8573.

31. Chin, J.W. 2017. Expanding and reprogramming the genetic code. Nature. 550: 53–60.

32. Lee, H.S., J. Guo, E.A. Lemke, R.D. Dimla, and P.G. Schultz. 2009. Genetic incorporation of a small, environmentally sensitive, fluorescent probe into proteins in Saccharomyces cerevisiae. J. Am. Chem. Soc. 131: 12921–12923.

33. Chatterjee, A., J. Guo, H.S. Lee, and P.G. Schultz. 2013. A Genetically Encoded Fluorescent Probe in Mammalian Cells. J. Am. Chem. Soc. 135: 12540–12543.

34. Cohen, B.E., T.B. McAnaney, E.S. Park, Y.N. Jan, S.G. Boxer, and L.Y. Jan. 2002. Probing Protein Electrostatics with a Synthetic Fluorescent Amino Acid. Science. 296: 1700–1703.

35. Kalstrup, T., and R. Blunck. 2013. Dynamics of internal pore opening in {KV} channels probed by a fluorescent unnatural amino acid. PNAS. 110: 8272–8277.

36. Aman, T.K., S.E. Gordon, and W.N. Zagotta. 2016. Regulation of CNGA1 Channel Gating by Interactions with the Membrane. J. Biol. Chem. 291: 9939–9947.

37. Soh, M.S., A. Estrada-Mondragon, N. Durisic, A. Keramidas, and J.W. Lynch. 2017. Probing the Structural Mechanism of Partial Agonism in Glycine Receptors Using the Fluorescent Artificial Amino Acid, ANAP. ACS Chem. Biol. 12: 805–813.

38. Sakata, S., Y. Jinno, A. Kawanabe, and Y. Okamura. 2016. Voltage-dependent motion of the catalytic region of voltage-sensing phosphatase monitored by a fluorescent amino acid. PNAS. 113: 7521–7526.

39. Dai, G., Z.M. James, and W.N. Zagotta. 2018. Dynamic rearrangement of the intrinsic ligand regulates KCNH potassium channels. J. Gen. Physiol. 150: 625–635.

40. Dai, G., and W.N. Zagotta. 2017. Molecular mechanism of voltage-dependent potentiation of KCNH potassium channels. eLife. 6: e26355.

41. Wulf, M., and S.A. Pless. 2018. High-Sensitivity Fluorometry to Resolve Ion Channel Conformational Dynamics. Cell Rep. 22: 1615–1626.

42. Zagotta, W.N., M.T. Gordon, E.N. Senning, M.A. Munari, and S.E. Gordon. 2016. Measuring distances between TRPV1 and the plasma membrane using a noncanonical amino acid and transition metal ion FRET. J. Gen. Physiol. 147: 201–216.

43. Wen, M., X. Guo, P. Sun, L. Xiao, J. Li, Y. Xiong, J. Bao, T. Xue, L. Zhang, and C. Tian. 2015. Site-specific fluorescence spectrum detection and characterization of hASIC1a channels upon toxin mambalgin-1 binding in live mammalian cells. Chem Commun. 51: 8153–8156.

44. Puljung, M., N. Vedovato, S. Usher, and F. Ashcroft. 2019. Activation mechanism of ATP-sensitive K+ channels explored with real-time nucleotide binding. eLife. 8: e41103.

45. Kalstrup, T., and R. Blunck. 2017. Voltage-clamp Fluorometry in Xenopus Oocytes Using Fluorescent Unnatural Amino Acids. JoVE J. Vis. Exp. : e55598–e55598.

46. Hsieh, T., N.B. Nillegoda, J. Tyedmers, B. Bukau, A. Mogk, and G. Kramer. 2014. Monitoring Protein Misfolding by Site-Specific Labeling of Proteins In Vivo. PLoS ONE. 9: e99395.

47. Mitchell, A.L., P.S. Addy, M.A. Chin, and A. Chatterjee. 2017. A Unique Genetically Encoded FRET Pair in Mammalian Cells. ChemBioChem. 18: 511–514.

48. Chen, P.R., D. Groff, J. Guo, W. Ou, S. Cellitti, B.H. Geierstanger, and P.G. Schultz. 2009. A Facile System for Encoding Unnatural Amino Acids in Mammalian Cells. Angew. Chem. Int. Ed. 48: 4052–4055.

49. Bacalum, M., B. Zorilă, and M. Radu. 2013. Fluorescence spectra decomposition by asymmetric functions: Laurdan spectrum revisited. Anal. Biochem. 440: 123–129.

50. Kruger, L.C., and L.L. Isom. 2016. Voltage-Gated Na+ Channels: Not Just for Conduction. Cold Spring Harb. Perspect. Biol. 8: a029264.

51. Bohnen, M.S., G. Peng, S.H. Robey, C. Terrenoire, V. Iyer, K.J. Sampson, and R.S. Kass. 2017. Molecular Pathophysiology of Congenital Long QT Syndrome. Physiol. Rev. 97: 89–134.

52. Bankston, J.R., M. Yue, W. Chung, M. Spyres, R.H. Pass, E. Silver, K.J. Sampson, and R.S. Kass. 2007. A Novel and Lethal De Novo LQT-3 Mutation in a Newborn with Distinct Molecular Pharmacology and Therapeutic Response. PLOS ONE. 2: e1258.

53. Oana Popa, M., A.K. Alekov, S. Bail, F. Lehmann-Horn, and H. Lerche. 2004. Cooperative effect of S4-S5 loops in domains D3 and D4 on fast inactivation of the Na+channel. J. Physiol. 561: 39–51.

54. Kirkton, R.D., and N. Bursac. 2011. Engineering biosynthetic excitable tissues from unexcitable cells for electrophysiological and cell therapy studies. Nat. Commun. 2: 300.

55. Dhamoon, A.S., and J. Jalife. 2005. The inward rectifier current (IK1) controls cardiac excitability and is involved in arrhythmogenesis. Heart Rhythm. 2: 316–324.

56. Chang, H.-K., J.-R. Lee, T.-A. Liu, C.-S. Suen, J. Arreola, and R.-C. Shieh. 2010. The Extracellular K+ Concentration Dependence of Outward Currents through Kir2.1 Channels Is Regulated by Extracellular Na+ and Ca2+. J. Biol. Chem. 285: 23115–23125.

57. Silva, J.R., and S.A.N. Goldstein. 2013. Voltage-sensor movements describe slow inactivation of voltage-gated sodium channels II: A periodic paralysis mutation in Nav1.4 (L689I). J. Gen. Physiol. 141: 323–334.

58. Blacker, T.S., and M.R. Duchen. 2016. Investigating mitochondrial redox state using NADH and NADPH autofluorescence. Free Radic. Biol. Med. 100: 53–65.

59. Teale, F.W.J., and G. Weber. 1957. Ultraviolet fluorescence of the aromatic amino acids. Biochem J. 65: 476–482.

60. Abriel, H., and R.S. Kass. 2005. Regulation of the Voltage-Gated Cardiac Sodium Channel Nav1.5 by Interacting Proteins. Trends Cardiovasc. Med. 15: 35–40.